Preprints (www.preprints.org) | NOT PEER-REVIEWED | Posted: 5 August 2016 doi:10.20944/preprints201608.0048.v1

Article

UAV Low Altitude Photogrammetry for Power Line Inspection

Yong Zhang [1], Xiuxiao Yuan [1,2,*], Yi Fang [1] and Shiyu Chen [1]

[1] Wuhan University, 129 Luoyu Road, Wuhan 430079, China; zyong@whu.edu.cn (Y.Z.); csy_hy@whu.edu.cn (S.C.)
[2] Collaborative Innovation Center of Geospatial Technology, Wuhan 430079, China
* Correspondence: yuanxx@whu.edu.cn; Tel.: +86-139-7111-3796

Abstract: When the distance between an obstacle and a power line is less than the discharge distance, a discharge arc can be generated, resulting in interruption of power supplies. Therefore, regular safety inspections are necessary to ensure safe operations of power grids. Tall vegetation and buildings are the key factors threatening the safe operation of extra high voltage transmission lines within a power line corridor. Manual or LiDAR based-inspections are time consuming and expensive. To make safety inspections more efficient and flexible, a low-altitude unmanned aerial vehicle remote-sensing platform equipped with optical digital camera was used to inspect power line corridors. We propose a semi-patch matching algorithm based on epipolar constraints using both correlation coefficient and the shape of its curve to extract three dimensional (3D) point clouds for a power line corridor. Virtual photography was used to transform the power line direction from approximately parallel to the epipolar line to approximately perpendicular to epipolar line to improve power line measurement accuracy. The distance between the power lines and the 3D point cloud is taken as a criterion for locating obstacles within the power line corridor automatically. Experimental results show that our proposed method is a reliable, cost effective and applicable way for practical power line inspection, and can locate obstacles within the power line corridor with measurement accuracies better than ±0.5 m.

Keywords: UAV remote sensing; power line inspection; dense matching; virtual photography; automatic detection of obstacles in power line corridor

---

1. Introduction

The expansion of the 500 kV extra high voltage (EHV) transmission line system for inter-provincial and large-span area power-supply tasks is presently a major project underway in China. To ensure safe operation of these lines is one of the important tasks for the power maintenance department at all levels. Buildings and tall plants such as eucalyptus and bamboo are typical obstacles threatening the safe operation of EHV transmission lines within power line corridors. Thus, power maintenance companies must devote a great deal of labor and material resources to power line corridor inspection, striving for timely elimination of these safety risks.

Existing methods for power line inspection fall into three categories; manual, airborne LiDAR, and unmanned aerial vehicle (UAV) inspection approaches. In manual ground-based inspection, each section in a segment of a power line corridor is assigned to a fixed inspection team. Manual visual interpretation is used to find, and record obstacles along the power line corridor. For the erection of EHV transmission lines, more remote routes are chosen in plain and hilly areas, while sunny slopes are chosen in hills or mountains. Consequently, it is difficult to conduct manual ground inspection. Obstacle interpretation depends on the conscientiousness and experience of inspection personnel, making inspection subjective. Moreover, manual inspection is dependent on visibility, so blind spots are unavoidable [1]. In airborne LiDAR power line inspection, a laser scanner is put onto a manned helicopter to obtain 3D point clouds of the objects and power line within the power line corridor. During post processing, the point cloud data is classified to extract objects and power lines within the line corridor. The distance between objects and power lines is used to locate obstacles. Existing research shows that although airborne LiDAR point clouds yield more accurate and less subjective inspection results than manual inspection [2], but expensive airborne LiDAR systems have high maintenance costs [3] in practical operation. This seriously restricts the application and popularization of this method. UAVs have the advantage of low cost and ease of operation, so are an attractive and popular option for power line inspection [4-6], and both fixed wing UAVs and multi-rotor UAVs have been adopted. UAV systems are flexible, digital cameras as well as video cameras are carried as UAV sensors [7]. Paper [8] comprehensively analyzed how computer vision technology is used in the operation and maintenance of transmission lines. Nevertheless, little attention has been paid to using low-altitude UAV images for accurate determination of distance between power lines and ground objects for automatic detection of obstacles found in power line corridors. In this paper, we propose a method of UAV power line inspection through automated detection of obstacles using photogrammetric approaches, thus fully exploiting the potential of UAV power line inspection.

To use the UAV to detect the obstacles within the power line corridor, three key problems need to be solved; 3D reconstruction of the ground of the power line corridor, power line measurement, and automatic recognition of obstacles. For ground reconstruction of the power line corridor, dense image matching techniques can be adopted to extract dense point clouds of the power line corridor; currently the extraction of dense point clouds from images obtained by low-altitude UAV is very active research area in fields of photogrammetry and computer vision [9-11]. In UAV power line inspection, image-matching algorithms must be adapted to ground conditions with dense vegetation. At the same time, algorithms must be capable of extracting tree canopies and buildings stably and reliably. When shooting images of a power line corridor, the flight direction of the UAV must be consistent with the direction of the electric power line. Thus, the direction of the power line will be approximately parallel to the direction of the image epipolar line. In a stereo mapping environment, a power line cannot be marked correctly, and it is difficult to control the measurement error. Zheng et al. [12] proposed a method for power line positioning under the constraint of vertical line, yet there still exist large measurement errors as a target moves up and down along the vertical line causing the measuring mark moves along the epipolar line on the left and right images. Sun et al. used a camera to shoot sequence images with GSD at about 10 cm; the 3D coordinates of the hang joint of the power line on a tower are determined by stereo images. The distance span between two towers, power line sag is modeled by catenary equation [13]. In this approach however, during modeling it is difficult to accurately account for the impact of the environmental temperature on the

 doi:10.20944/preprints201608.0048.v1

power line sag, thus, sag is not accurately reflected during power line inspection. Obstacles within the corridor not only appear just below the power line, but also around the power line. Thus, automatic recognition must identify potentially dangerous obstacles within a certain safety range.

To solve these three problems, semi patch matching based on epipolar constraints (SPMEC) was adopted to extract the dense point clouds for 3D reconstruction of ground objects in a power line corridor. Virtual photography is adopted to improve power line stereo measurement accuracy. A virtual camera is arranged in a proper position perpendicular to the direction of the route on both sides of the real photography station. The images shot with a real camera are mapped to a virtual camera, which changes the direction of the power line from approximately parallel to being approximately perpendicular with the epipolar line for greater accuracy in stereo measurements. Finally, a power line is used as a bus bar, and a buffer space analysis is carried out according to the safety distance set in specification code, so obstacles can be detected automatically.

2. Automatic Detection of Obstacles in Power Line Corridors

All the objects in the power line corridor with a distance to the power line less than the safety distance are defined as obstacles. If the 3D surface reconstruction of a power line corridor is complete, the power line sag measured, and a safe distance threshold given, then obstacles can be automatically located. Low-altitude UAV images, obtained after GNSS-supported aerial triangulation [14], are the objects to be processed. Semi patch matching based on epipolar constraints was adopted to extract the dense point clouds within the corridor for 3D reconstruction of the ground objects including canopies, buildings, and other ground attachments. The stereo image pair composed of virtual photography and real images was used for automatic measurement of the power line sag. Finally, along the power line direction at a set interval, we calculate the distance between the power line sag and the surface point cloud to determine whether it is within the safe distance range. An obstacle is identified when ground points are located within a distance less than the prescribed safety distance threshold.

2.1. Semi Patch Matching Algorithm Based on Epipolar Constraints

In this paper, epipolar images are the processing unit and a coarse to fine image matching strategy was adopted. In our proposed method, under the initial parallax constraint, a large matching window, searches a one-dimensional image along the epipolar line , is used to extract the coarse matching seed points. If a parallax is continuous within an object, and the same object has a consistent texture in the image, then the coarse matching seed point considered as the center of the fine matching window. In the segmented image, based on the segmented object of the seed point, a patch matching constraints is constructed (the segmentation result of an object only occupies a part of the area within $w \times w$ pixels range around the seed point, so it is called a semi patch). Then, the initial parallax of the points to be matched within the semi patch is determined according to the geometric conditions of the semi patch. A one-dimensional search is conducted within a smaller search range. Finally, an outlier detection algorithm extremely sensitive to local elevation eliminates the mismatched points.

1) Construction of Triangulation Network Controlled by Initial Parallax of Stereo Image Pairs

Relative orientation is conducted by using the image tie points automatically measured in the stereo image pairs, and epipolar image pairs are generated. Meanwhile, the tie points are projected

 doi:10.20944/preprints201608.0048.v1

to the epipolar image, obtaining the coordinate and parallax of the tie point $p_i(x, y)$ (i=1,2,…,n) in the left epipolar image, represented by P_{ei} (x_{ei}, y_{ei}, d_{ei}). According to the generation algorithm of an irregular triangulation network [15], a triangulated irregular network (TIN) is constructed for n relative orientation points, and corresponding pseudo color is given to the triangle vertexes according to the difference of the parallax value d_{ei}. A parallax TIN is shown in Figure 1.

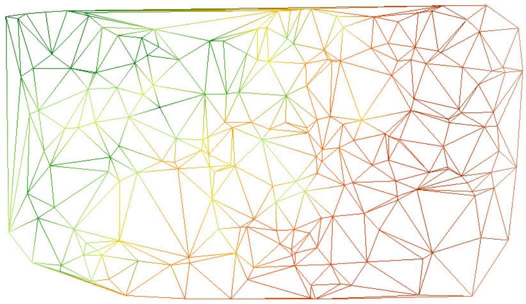

Figure 1. Triangulation Irregular Network of Initial Parallax

In Figure 1, triangle vertexes are composed of relative orientation points, and corresponding pseudo color is given to the triangle vertexes according to the difference of the parallax value.

2）Stereo Image Matching Based on a Parallax Control Grid

First, a parallax control grid P_{egi} (x_{egi}, y_{egi}) is set to an interval of 15 pixels in the left epipolar image. Then, grid points are put into a TIN controlled by initial parallax, and the triangle $\Delta P_{ei}P_{ej}P_{ek}$ where P_{egi} lays is obtained. Bilinear interpolation is conducted on the parallaxes of the three vertices of the triangle [16] to obtain the initial parallax of P_{egi}. Then 61×61 pixels are used as the matching window. Slide within [x_{egi}-100, x_{egi}+100] in the right epipolar image; for each pixel, the normalized correlation coefficient of the corresponding window is calculated according to Eq. (1), and a correlation coefficient curve is generated as shown in Figure 2.

$$\rho_{c,r} = \frac{\sum_{i=0}^{n}\sum_{j=0}^{n}[g_1(j,i) - \bar{g}_1]\times[g_2(j+c,i+r)-\bar{g}_2]}{\sqrt{\sum_{i=0}^{n}\sum_{j=0}^{n}[g_1(j,i) - \bar{g}_1]^2\times\sum_{i=0}^{n}\sum_{j=0}^{n}[g_2(j+c,i+r)-\bar{g}_2]^2}} \quad (1)$$

where (c, r) are the coordinates of the corresponding pixel of the center point pixel of the matching window in the right epipolar image; and the values $\bar{g}_1$ and $\bar{g}_2$ are the average gray levels of the corresponding matching window in the left and right epipolar image, respectively. The size of the matching window is n and i, j are the line number and column number of the pixels within the matching window; and $g_1(j,i)$ and $g_2(j,i)$ are the gray values of the pixel (j, i) in the left and right epipolar image, respectively.

Preprints (www.preprints.org) | NOT PEER-REVIEWED | Posted: 5 August 2016 doi:10.20944/preprints201608.0048.v1

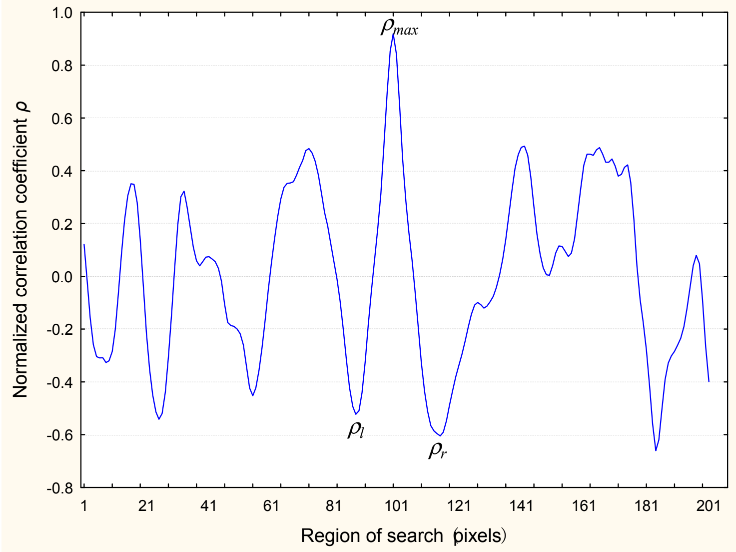

Figure 2. Correlation Coefficient Curve

In Figure 2, $\rho_{\max}$ is the peak value of the normalized correlation coefficient of the matching window and searching window at the corresponding pixel. ρ_l and ρ_r are the normalized correlation coefficients of the lowest points of the monotone decrease on both sides of the peak value respectively. To determine if the matching is successful we apply Eq. (2) as follows:

$$\begin{cases} \textit{successful}, & \text{when } \rho_{\max} \geq 0.9 \\ \textit{successful}, & \text{when } \rho_{\max} < 0.9 \text{ and } |\rho_l - \rho_r| < 0.2 \text{ and } |l_l - l_r| < 5.0 \text{ and } [\rho_{\max} - (\rho_l + \rho_r)/2] \geq 0.6 \\ \textit{failed}, & \text{else} \end{cases} \quad (2)$$

where l_l and l_r are the distances between the peak value and the lowest points on both sides of the peak value respectively, in pixels.

It can be seen from Eq. (2), in contrast to most matching algorithms based on a normalized correlation coefficient, when design similarity criterion, we use not only the value of the normalized correlation coefficient but also the curve characteristics of the correlation coefficient. During image correlation when sliding the matching window, if the corresponding image point is found in the search region of the right image, then the correlation coefficient will change following a law from small to large and then from large to small as the matching window gets closer and moves far away from corresponding point. Isolated peaks are evident in the data; two sides of the peak value are approximately symmetrical (as shown in Figure 2). In the Eq. (2), $|\rho_l - \rho_r| < 0.2$ and $|l_l - l_r| < 5.0$ are used respectively to constrain the symmetry of both sides of the correlation coefficient peak, $[\rho_{\max} - (\rho_l + \rho_r)/2] \geq 0.6$ is used to constrain the distinctiveness of the correlation coefficient peak. Many experiments show that compared to simple correlation coefficient threshold methods, the similarity measure adopted in this paper can improve the reliability of image matching results and the density of the corresponding image points.

3) Semi Patch Dense Image Matching

Segment the left epipolar image, and the segmentation result is shown in Figure 3.

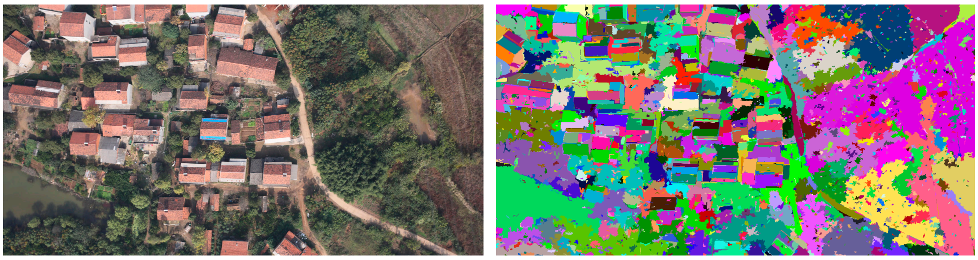

(a) Image to be Segmented (b) Segmentation Result

Figure 3. Image Segmentation Result

For a pixel p_i to be matched, $\boldsymbol{P}=\{p_1,p_2,\cdots,p_n\}$, set of grid nodes located in the corresponding segmented area within the parallax regular gird network, and $\boldsymbol{D}=\{d_1,d_2,\cdots,d_n\}$ parallax of pixels in the set, can be obtained. Because the pixels in the same-segmented areas have similar texture features in a local neighborhood of objective space, assuming that the regular object surface has a consistent image texture, $\pi(p_x,p_y,d)$ the parallax space plane can be constructed by using the image point coordinates within the set $\boldsymbol{P}$ and the corresponding parallax. Put p_i into π, the plane equation, then d_i, the initial parallax, can be obtained. Then taking 11×11 pixels as a matching window, slide within [x_{egi}-20, x_{egi}+20] in the right epipolar image. For each pixel, the normalized correlation coefficient of the corresponding window is calculated according to Eq. (1). Then we determine if the matching was successful according to Eq. (2).

4) Eliminating Mismatched Points

Assume that the point to be matched $p(x, y, d)$, the matching results $\boldsymbol{T}$ is expressed as the set of p. If the set has a total of n points, the distance between any two points in the set can be expressed as:

$$l(i,j)=\sqrt{(x_i-x_j)^2+(y_i-y_j)^2+(d_i-d_j)^2} \qquad \left(p_i,p_j\in\boldsymbol{T}\right) \tag{3}$$

Assume that the probability of mismatched points in the set of matched points is b, so the number of correctly matched points that may include in the point set is $M=(1.0-b)\times n$. For o, any point in $\boldsymbol{T}$, if L, the distance, is given, N, the number of points within the range with o as the origin, L as the radius can be obtained. If $N<M$, o is the mismatched point; otherwise, it is correctly matched point. Thus, the criterion used in this paper depends on two parameters of b and L. Experiments have shown that, it is more appropriate to take $b=20\%$ and $L=\sqrt{2(w^2+h^2)}$ (w and h represent the width and height of the external rectangle corresponding to the convex hull of the image plane of $\boldsymbol{T}$, respectively.

Taking the epipolar images as objects to be matched, the image tie points obtained by GNSS-supported aerial triangulation were used as an initial condition; a triangular irregular network controlled by initial parallax was constructed. After parallax controlled grid interpolation, semi-patch matching and mismatched points eliminating, ground dense point clouds can be obtained as shown in Figure 4. The texture color of the point clouds are taken from the left epipolar image.

 doi:10.20944/preprints201608.0048.v1

Figure 4. Dense 3D Point Clouds Extracted by SPMEC

As seen in Figure 4, the SPMEC achieves 3D ground reconstruction of the power line corridor, with morphologically intact canopies, regular building edges, and clear small building components such as chimneys and solar water heaters, providing an accurate digital surface model for automated detection of the obstacles within power line corridors.

2.2. Stereo Measurement of Power Line Based on Virtual Photography

1) Virtual Photography

Assume that exterior orientation elements of the real image are X_{s1}, Y_{s1}, Z_{s1}, ϕ_1, ω_1, κ_1. If the exterior orientation elements of the given virtual image are X_{s2}, Y_{s2}, Z_{s2}, ϕ_2, ω_2, κ_2, the image point (x_2, y_2) of the corresponding image point with image point (x_1, y_1) are as follows:

$$\begin{bmatrix} X \\ Y \\ Z \end{bmatrix} = \lambda_1 \boldsymbol{R}_1 \begin{bmatrix} x_1 \\ y_1 \\ -f \end{bmatrix} + \begin{bmatrix} X_{s1} \\ Y_{s1} \\ Z_{s1} \end{bmatrix} = \lambda_2 \boldsymbol{R}_2 \begin{bmatrix} x_2 \\ y_2 \\ -f \end{bmatrix} + \begin{bmatrix} X_{s2} \\ Y_{s2} \\ Z_{s2} \end{bmatrix} \quad (4)$$

where (X, Y, Z) are ground coordinates of object points; f is the principal distance of the camera; λ_1 and λ_2 are scale factors that can be taken as m, the denominator of photographic scale; $\boldsymbol{R}_1$ and $\boldsymbol{R}_2$ are the orthogonal transformation matrixes composed by two image exterior angular elements, respectively.

Then equation (4) can be sorted as:

$$\begin{bmatrix} x_1 \\ y_1 \\ -f \end{bmatrix} = \frac{\lambda_2}{\lambda_1} \boldsymbol{R}_1^{-1} \boldsymbol{R}_2 \begin{bmatrix} x_2 \\ y_2 \\ -f \end{bmatrix} + \frac{1}{\lambda_1} \boldsymbol{R}_1^{-1} \begin{bmatrix} X_{s2} - X_{s1} \\ Y_{s2} - Y_{s1} \\ Z_{s2} - Z_{s1} \end{bmatrix} \quad (5)$$

After exterior orientation elements of the real image are obtained by GNSS-supported aerial triangulation, the exterior linear elements of the virtual image are obtained as $X_{s1} + B_X$、 $Y_{s1} + B_Y$、 Z_{s1}, and $\lambda_1 = \lambda_2 = m$, if a virtual camera is put at $(B_X, B_Y, 0)$, equation (5) can be simplified as follows:

$$\begin{bmatrix} x_1 \\ y_1 \\ -f \end{bmatrix} = \boldsymbol{R}_1^{-1} \boldsymbol{R}_2 \begin{bmatrix} x_2 \\ y_2 \\ -f \end{bmatrix} + \frac{1}{m} \boldsymbol{R}_1^{-1} \begin{bmatrix} B_X \\ B_Y \\ 0 \end{bmatrix} \quad (6)$$

Equation (6) shows the coordinate relation between the virtual image and the real image. According to Eq. (6), projective coordinates of each pixel of the virtual image in the real image can

Preprints (www.preprints.org) | NOT PEER-REVIEWED | Posted: 5 August 2016 doi:10.20944/preprints201608.0048.v1

be calculated. After gray resampling [17], virtual photography can be completed.

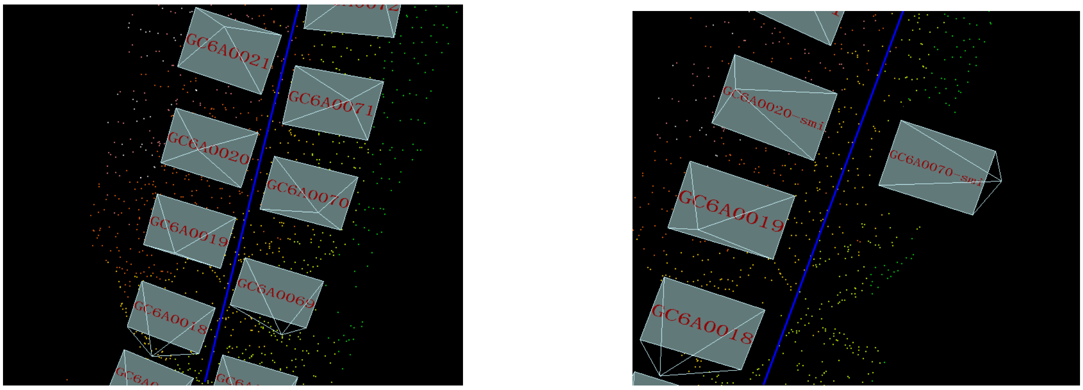

(a) Schematic diagram of real image position (b) Schematic diagram of virtual image position

Figure 5. Virtual image position on both sides along the power line

As shown in Figure 5, there are two flight strips along power line. Pyramids stand for the position and orientation of the images. Pseudo color points are the pass points. Take an image, such as image CGA0020, on the left side of the powerline for an example, we place a virtual camera on the exact position of the real image with orientation parameters such that φ_2=0, ω_2=0, κ_2=κ_1. Apply equation (6) to get the virtual image CGA0020-smi shown in Figure 5(b). For the image on the right side of the powerline, such as CGA0070, we calculate its virtual image position using the direction of the left side flight strip and the distance *d* between both flight strips. The virtual image position should be at the perpendicular line to the direction of left side flight strip with a distance of *d*. The orientation parameters are φ_2=0, ω_2=0, κ_2=κ_1. Also apply equation (6) to get the virtual image CGA0070-smi shown in Figure 5(b). When apply virtual photography for the images on left side, *Bx* and *By* in equation (6) equal to zero because we place the virtual camera on the exact position of the real image. Hence, the stereo measurement accuracy of virtual image is not affect by terrain relief. For images on the right side, the photographic scale of every pixel on the virtual image is different because of the change of image position. Since we apply a fixed mean photographic scale in equation (6), there will introduce some imaging error cause by terrain relief. According to [18], the error of every single pixel can be calculated using equation (7):

$$\begin{cases} \Delta x = fX_{vs} \dfrac{H_0 / H}{(H - H_0)} \\ \Delta y = fY_{vs} \dfrac{H_0 / H}{(H - H_0)} \end{cases} \tag{7}$$

Where f denotes for focal length of the camera, H_0 denotes for the ground target height to the virtual photography, H denotes for the flight height, and X_{VS}, Y_{VS} denote for the distance between the virtual image projective center and the real image projective center.

According to Eq. (7), when f is 35 mm, H_0 is 90 m, and H is 300 m, the displacement of pixel on virtual image is approximately 0.28 pixel, which is at the same order of the magnitude of the random error caused by manually powerline stereo measure, hence can be ignored.

2) Manual and Automatic Measurement of Power Line

The base line direction of the stereo image pair, composed by the real image and the virtual image, is perpendicular to the flight direction, and flight direction is approximately parallel to the direction of the power line. Therefore, the epipolar direction of the stereo image pairs is approximately perpendicular to the direction of the power line, which can improve the stereo observation accuracy. In general, the vertical distance between the power line and the ground is between 20 m and 40 m. During manual stereo observation, due to lack of focus reference, it is easy to make the eyes focus on the ground, hence difficult to align the stereo mark at the power line. When using a virtual stereo image pair, and the measuring mark moves in the epipolar direction, the intersection point of the epipolar line and power line is the corresponding point on power line. The only thing required for power line measurement is to make sure that the left and right measuring marks align at the power line at the same time. In this way, power line sag can be measured accurately without stereo observation. However, this method is not only suitable for manual stereo measurement of power lines, but is also the theoretical foundation for fully automated measurement of power lines. Experiments by Li et al. have shown that, it is entirely feasible to extract power lines from aerial images with GSD better than 5cm [19]. After vectorize the extracted powerline on both image of the virtual stereo image pair, we calculate intersection points of the corresponding epipolar line and the powerline along the perpendicular direction of the epipolar line at a certain close-enough interval. We calculate the 3D coordinates of these corresponding points using forward intersection. Then the powerline can be accurately measured.

2.3. Automatic Detection of Obstacles in Power Line Corridor

After extracting the power line and 3D point clouds of power line corridor, we take the power line as the bus line and construct a spatial buffer zone around power line with a safe distance of *r*. An obstacle can be located when 3D point clouds intersect with the spatial buffer zone. The process of locating an obstacle is shown in Figure 6.

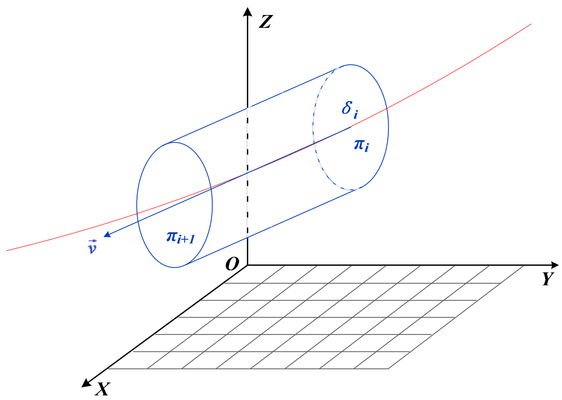

Figure 6. Diagram of Principle for Automatic Obstacle Detection

In Figure 6, the power line is divided into n segments with δ as step distance. The terminals can be expressed as $\delta_1, \delta_2, \cdots, \delta_n, \delta_{n+1}$. When δ is small enough, each segment can be regarded as a straight line. δ, the step distance, and $\vec{v} = [A \quad B \quad C]^{\mathrm{T}}$, tangential direction at δ_i, can be obtained by the two adjacent terminals $\delta_i(X_i, Y_i, Z_i)$ and $\delta_{i+1}(X_{i+1}, Y_{i+1}, Z_{i+1})$:

$$\begin{cases} \delta = \sqrt{(X_i - X_{i+1})\cdot(X_i - X_{i+1}) + (Y_i - Y_{i+1})\cdot(Y_i - Y_{i+1}) + (Z_i - Z_{i+1})\cdot(Z_i - Z_{i+1})} \\ \vec{v} = [A \quad B \quad C]^{\mathrm{T}} = [X_{i+1} - X_i \quad Y_{i+1} - Y_i \quad Z_{i+!} - Z_i]^{\mathrm{T}} \end{cases} \tag{8}$$

As shown in Figure 6, if the straight line of cross point δ_i in the direction $\vec{v}$ is l_i, then the planes of δ_i and its adjacent terminal, π_i and π_{i+1}, taking $\vec{v}$ as normal vector can be expressed by Eq. (9a) and Eq. (9b), respectively; and the sphere with δ_i as center and r, safety distance

Preprints (www.preprints.org) | NOT PEER-REVIEWED | Posted: 5 August 2016 doi:10.20944/preprints201608.0048.v1

threshold, as radius can be expressed by Eq. (9c).

$$A(X-X_i)+B(Y-Y_i)+C(Z-Z_i)=0 \tag{9a}$$

$$A(X-X_{i+1})+B(Y-Y_{i+1})+C(Z-Z_{i+1})=0 \tag{9b}$$

$$(X-X_i)^2+(Y-Y_i)^2+(Z-Z_i)^2=r^2 \tag{9c}$$

For an arbitrary point (X_0, Y_0, Z_0) on the plane π_i, if it satisfies Eq. (9c), then the point will be on the intersection line of the sphere and the plane π_i, forming a circle Θ. A cylindrical surface Φ shown in Eq. (9d) takes Θ as its directional line and a straight line as its bus line, where the straight line passes through (X_0, Y_0, Z_0) and takes $\vec{v}$ as its direction.

$$\begin{cases} A(X_0-X_i)+B(Y_0-Y_i)+C(Z_0-Z_i)=0 \\ (X_0-X_i)^2+(Y_0-Y_i)^2+(Z_0-Z_i)^2=r^2 \\ \dfrac{X-X_0}{A}=\dfrac{Y-Y_0}{B}=\dfrac{Z-Z_0}{C}=t \end{cases} \tag{9d}$$

Simplify equation (9d) and after eliminating the variants X_0, Y_0, Z_0, the cylindrical surface Φ can be expressed as:

$$(At-X+X_i)^2+(Bt-Y+Y_i)^2+(Ct-Z+Z_i)^2=r^2 \tag{10}$$

where $t=\dfrac{A(X-X_i)+B(Y-Y_i)+C(Z-Z_i)}{A^2+B^2+C^2}$, which can be obtained by putting in the coordinates of point cloud (X, Y, Z).

If there exist points in digital surface point clouds that are at Φ or inside the cylinder formed by the planes π_i and π_{i+1}, satisfying the following condition:

$$\begin{cases} (At-X+X_i)^2+(Bt-Y+Y_i)^2+(Ct-Z+Z_i)^2 \le r^2 \\ \dfrac{\left|AX+BY+CZ-(AX_i+BY_i+CZ_i)\right|+\left|AX+BY+CZ-(AX_{i+1}+BY_{i+1}+CZ_{i+1})\right|}{\sqrt{A^2+B^2+C^2}} \le \delta \end{cases} \tag{11}$$

Then these points are considered as obstacles. The distance between these points and the straight line is the distance between the obstacles and the power line. In this way, the exact position of the detected obstacles is determined.

3. Results and Discussion

In order to verify the validity of the proposed method, the authors wrote an experimental program using the VC++ language. A section of a 220 kV power line about 16.5 km in length in Yichang, Hubei was selected for an inspection experiment. A fixed wing UAV (shown in Figure. 7) with a Nikon D810 camera (focal length 50 mm, CCD pixel size 4.88 µm) was adopted for low-altitude photography of the power line corridor.

Preprints (www.preprints.org) | NOT PEER-REVIEWED | Posted: 5 August 2016 doi:10.20944/preprints201608.0048.v1

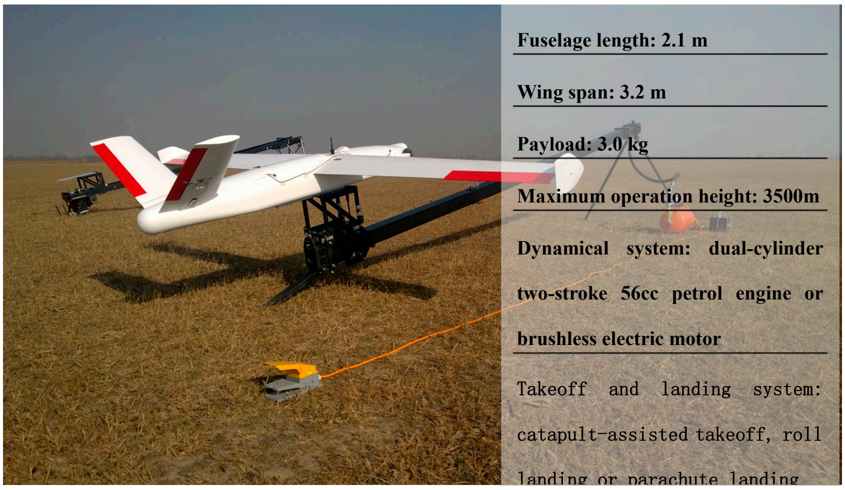

Figure 7. Diagram of fixed wing UAV

The GSD was about 3.5 cm, two sorties were flown, and 1066 images obtained. The images are clear, and the contrast is moderate, which can meet the requirements for power line inspection. All the images were processed according to the procedures mentioned in Section 2. Ground 3D point clouds and power line sag of some segments are shown in Figure 8.

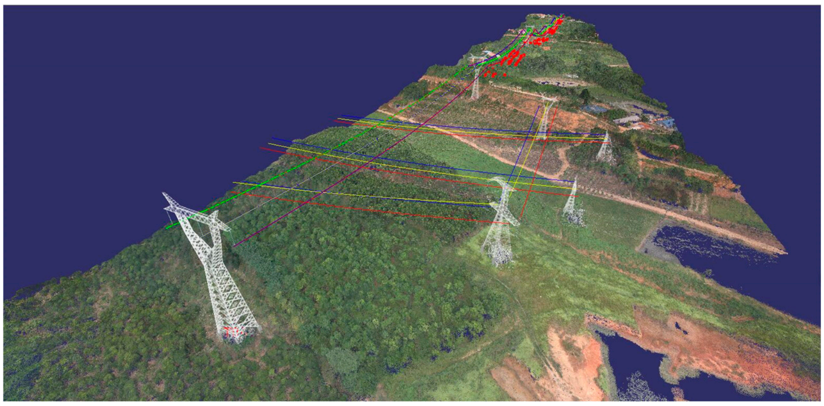

Figure 8. Diagram of Ground 3D Point Clouds and Power Line Sag within the Power Line Corridor

In Figure 8, the ground 3D point clouds were extracted by SPMEC, the red points are obstacles, the red, yellow and blue wires are obtained by virtual photography and manual stereo measurement. The towers are existing 3D models put in the scene, to make it more intuitive.

3.1. Detection of Obstacles in Power Line Corridor

Based on the results shown in Figure 8, when the safety distance threshold between the power line and 3D point clouds was set to 15m, the locations of obstacles were listed in Table 1 using method mentioned in section 2.3, one obstacle is shown in Figure 9.

 doi:10.20944/preprints201608.0048.v1

Table 1. Distribution of Some Obstacles within Power Line Corridor (safety distance threshold is 15 m)

Tower Section	Position of the Obstacle (m)	Distance between the Obstacle and the Power Line (m)
K182～K183	133.0—135.0	14.658
	180.5—185.0	13.990
	188.5—189.0	14.865
	201.5—268.0	11.182
	119.5—123.5	12.137
	191.5—201.5	12.518
	204.0—206.0	13.809

Table 1 lists number of the towers, the distance between the obstacles and K182 tower, and the distance between the obstacles and power lines.

Figure 9. Diagram of an obstacle within the Power Line Corridor

As shown in Figure 9, an obstacle has certain continuity in space. Therefore, in Table 1, the position of the obstacle is expressed as a continuous range. The minimum distance within this rang is taken as the distance between an obstacle and the power line. The measurement accuracy of the obstacles will be further verified.

Because the power line selected for experiment is operational, it is impossible to measure the distance of the power line sag and the objects directly. It is also difficult to aim at the power line with a total station instrument. Consequently, in this paper, two methods are used to check the accuracy of power line inspection and measurement of ground point clouds. A field investigation was conducted and the results were reviewed by manual inspection to confirm the validity of the method and the accuracy of the automatic detection.

Method 1: A Trimble TX8 ground laser scanner was used for 3D scanning of the tower K182 and its power line. Firstly, the GPS Real-time kinematic (RTK) was used for accurately locating the position of the TX8 scanner, and then, the orientation point coordinates of the TX8 were measured, and equipment orientation was completed. The 3D laser point cloud was obtained by 3D scanning of the TX8 as shown in Figure 10. We overlaid the point cloud data for the power line as collected from the TX8 scanner and the power line vectors generated by stereo capture as put forward in this paper. Taking the power line sag captured by the TX8 as the “ground trues”, with an interval of 1 m, the gravity center of the section of the point cloud of the power line and the intersection point of the power line and the section were collected to calculate the elevation difference between the gravity center and the intersection point. Then, the error in the elevation difference was taken as criterion to evaluate the measurement precision of the power line. Several sampling points and the elevation differences are listed as shown in Table 2.

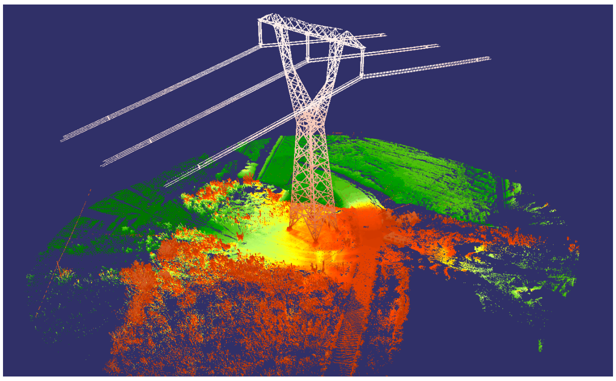

Figure 10. Diagram of Point Cloud Scanned by Laser 3D Scanner at K182

Table 2. Distribution of Elevation Difference of Sampling Points in Power Line Profile (Unit: m)

Elevation of 3D Point Cloud	Elevation of Stereo Measurement	Elevation Difference	Elevation of 3D Point Cloud	Elevation of Stereo Measurement	Elevation Difference
138.313	138.720	0.407	128.632	128.053	-0.579
135.709	135.644	-0.065	129.721	129.765	0.044
133.423	133.632	0.210	131.185	130.857	-0.328
131.511	131.414	-0.097	133.024	133.308	0.284
129.975	130.411	0.436	135.237	135.683	0.446
128.813	128.804	-0.009	137.826	137.376	-0.450
128.027	128.164	0.137	140.790	141.163	0.373
Root Mean Square Error of the Elevation Difference: 0.326					

It can be seen from Table 2 that, the virtual photography approach adopted in this paper transforms the direction of the power line from approximately parallel to the epipolar direction into being approximately perpendicular to the epipolar direction, so that the measuring mark is accurately aligned at the power line while moving along the epipolar line. Measurement accuracy of the elevation reached ±0.326 m on the ground.

Method 2: 20 distinct ground objects were selected within the power line corridor, whose 3D ground coordinates were measured in the field by GPS RTK. The accuracy of planimetry and elevation both reached the cm level in the ground [20], so were regarded as "ground trues". The 3D coordinates obtained in the stereo measuring environment were compared with these true values one by one to evaluate the accuracy of the ground point cloud extracted. Differences between the coordinates of all the checking points are listed in Table 3.

 doi:10.20944/preprints201608.0048.v1

Table 3. Difference of Coordinates of the Checking Points (Unit: m)

Checking Point	*X*	*Y*	Planimetry	Elevation
1	0.020	-0.034	0.040	0.383
2	0.043	-0.014	0.045	0.126
3	0.043	0.007	0.044	0.103
4	-0.090	-0.015	0.091	0.278
5	-0.011	-0.076	0.077	0.156
6	-0.017	0.036	0.039	-0.182
7	-0.129	-0.088	0.156	0.408
8	0.084	-0.003	0.084	-0.133
9	-0.006	-0.001	0.006	0.005
10	0.053	0.081	0.097	0.421
11	0.013	-0.180	0.180	0.177
12	0.017	-0.024	0.029	0.162
13	-0.005	-0.099	0.100	0.276
14	0.013	0.124	0.125	-0.578
15	-0.119	-0.006	0.119	0.269
16	-0.045	0.082	0.094	-0.391
17	-0.040	0.020	0.045	-0.234
18	-0.053	-0.059	0.079	0.356
19	0.086	-0.014	0.087	-0.196
20	-0.181	0.129	0.222	-0.442
Maximum Difference	-0.181	-0.180	0.222	-0.578
Root Mean Square Error	0.071	0.075	0.103	0.302

It can be seen from Table 3, that the coordinates of distinct objects obtained by manual observation in the stereo measuring environment are quite consistent with the coordinates measured in the field. The maximum differences of the planimetry and elevation of the point cloud are 0.222 m and -0.578 m, and root mean square errors are ±0.103 m and ±0.302 m, respectively. Further analysis shows that if the measurement error of "ground trues" was deducted, the elevation measurement accuracy obtained by the two methods is basically the same. Consequently, the results in Table 3 can be regarded as evidence to evaluate the accuracy of our method for extracting power line and ground point clouds.

In addition, the measuring principle of image dense matching process is the same as manual stereo measure. Using image matching to replace the manual stereo measure with human eyes, and using parabolic fitting during image matching to further increase accuracy, image matching accuracy can achieve ±0.29 pixels [21], while significantly decreases the manual measure error. Hence, compared with manual stereo measure, image dense matching has a higher accuracy.

It can be seen from Tables 2 and 3 that the elevation accuracies of power line sag and ground 3D point clouds was ±0.326 m and ±0.302 m, respectively. Based on error propagation principles, the relative elevation difference accuracy of power line sag and ground 3D point cloud was estimated at ±0.444 m. Our proposed method achieved distance-measuring accuracy better than ±0.5 m, such accuracy meets the requirements of power line inspection.

4. Conclusions

In this paper, an automatic method for inspecting power line corridors for obstacles was proposed, using UAV low-altitude digital images. The images processed by the GNSS-supported aerial triangulation were the input, and obstacle distribution report was the output. We focused on solving three problems: 3D reconstruction of the ground surface of the power line corridor, measurement of power line sag, and automatic recognition of obstacles. According to the similarity measurement which takes the normalized correlation coefficient and the shape of the coefficient curve into consideration, dense point clouds of canopies and buildings with regular outline can be extracted by SPMEC in rural areas with lush vegetation. Even small building components such as the chimneys and solar water heaters can be clearly expressed. Virtual photography was used to build a measurable stereo image pairs, transforming the power line approximately parallel to direction into being approximately perpendicular to it, which has effectively improved detection accuracy of the power lines. Experimental results show that our approach proposed can automatically find and accurately locate the obstacles in the power line corridors with measurement accuracies better than ±0.5 m, providing a new means for quantitative inspection of obstacles to the safe operation of ultra-high voltage transmission lines. However, further experimental research and engineering development must be done to refine and improve fully automatic epipolar-constraint-based power line inspection.

Supplementary Materials: The following are available online at http://pan.baidu.com/s/1dFqJgy9, Video S1: Power line inspection demo.

Acknowledgments: This work has been supported by the National Key Developing Program for Basic Sciences of China (Grant No. 2012CB719902) and National Natural Science Foundation of China (Grant No. 41371432).

Author Contributions: Mr. Yong Zhang developed the algorithm and conducted the primary data analysis, as well as crafting the manuscript. Prof. Xiuxiao Yuan advised on and contributed to the data analysis, as well as provided remote sensing experience, and significant editing of the manuscript. Mr. Yi Fang and Mr. Shiyu Chen carry out the experiments, advised on research question generation, and reshaping of the manuscript.

Conflicts of Interest: The authors declare no conflict of interest.

References

1. Mu Chao, "Research on extraction method of power line corridor feature based on multi remote sensing data," Ph.D. dissertation, Dept. PE&RS, Wuhan Univ., Wuhan, CHN, 2010.
2. Kuhnert K D, Kuhnert L, "Light-weight sensor package for precision 3D measurement with micro UAVs E.G. power-line monitoring," International Archives of the Photogrammetry, Remote Sensing and Spatial Information Sciences, vol. XL-1/W2, pp.235—240, Sep. 2013.
3. Ahmad J, Malik A S, Xia L, et al., "Vegetation encroachment monitoring for transmission lines right-of-ways: a survey," Electric Power Systems Research, vol. 95, no. 1, pp. 339—352, 2013.
4. Chang an, Wang Chunyang, "Mission planning of the flying robot for powerline inspection," Progress in Natural Science, vol.19, no.10, pp. 1357—1363, 2009.
5. Mulero-Pázmány M, Negro J J, Ferrer M, "A low cost way for assessing bird risk hazards in power lines: Fixed-wing small unmanned aircraft systems," Journal of Unmanned Vehicle Systems, vol. 2, no. 1, pp. 5—15, 2014.
6. Cerón A, Iván F. Mondragón, Prieto F, "Visual based navigation for power line inspection by using virtual environments," SPIE/IS&T Electronic Imaging. International Society for Optics and Photonics, vol. 9406, pp. 94060J-1—7, 2015.

7. González-Jorge et al., “UAV potogrammetry monitoring application to the monitoring of rubble mound breakwaters,” J. Perform. Constr. Facil., vol. 30, no. 1, pp. 04014194, 2016.
8. Miralles F, Pouliot N, Montambault S, "State-of-the-art review of computer vision for the management of power transmission lines," IEEE International Conference on Applied Robotics for the Power Industry (CARPI), vol. 32, no. 12, pp. 1805—9, 2015.
9. Hirschmüller H, "Accurate and efficient stereo processing by semi-global matching and mutual information," IEEE Computer Society Conference on CVPR, vol. 2, no. 2, pp. 807—814, 2005.
10. Yasutaka F, Jean P, "Accurate, dense, and robust multiview stereopsis," IEEE Transactions on Pattern Analysis and Machine Intelligence, vol. 32, no. 8, pp. 1362—76, 2010.
11. Bleyer M, C. Rhemann, and C. Rother, "Patchmatch stereo - stereo matching with slanted support windows," BMVC, pp. 14.1—14.11, 2011.
12. Zheng S Y, Hu H L, Huang R Y, et al. "Realtime ranging of power transmission line," Geomatics and Information Science of Wuhan University, vol. 36, no. 6, pp. 704—707, 2011.
13. Sun C, Jones R, Talbot H, et al., "Measuring the distance of vegetation from powerlines using stereo vision," ISPRS Journal of Photogrammetry and Remote Sensing, vol. 60, no. 4, pp. 269—283, 2006.
14. Yuan X X, "A novel method of systematic error compensation for a position and orientation system," Progress in Natural Science, vol. 18, no. 8, pp. 953—963, 2008.
15. Shewchuk, Jonathan Richard, "Delaunay refinement algorithms for triangular mesh generation," Computational Geometry, vol. 22, no. 1-3, pp. 21—74, 2002.
16. Gribbon K. T., Bailey D. G., "A novel approach to real-time bilinear interpolation," IEEE International Workshop on Electronic Design, Test and Applications, Proceedings, Delta IEEE, pp. 126—131,2004.
17. Jensen J R, and K. Lulla, "Introductory digital image processing: a remote sensing perspective," Geocarto International, vol. 2, no. 1, pp. 382—382, 1986.
18. Liu X L, “Principle and Technology of Omo-array Digital Aerophotogrammetry”, Henan science and Technology Publishing House, 2013.
19. Li C Y, Yan G J, Xiao Z Q, et al., "Automatic extraction of power lines from aerial images," IEEE Geoscience & Remote Sensing Letters, vol. 4, no. 3, pp. 387—391, 2007.
20. Timothy R. Lemmon, George P. Gerdan, "The influence of the number of satellites on the accuracy of RTK GPS positions," Australian Surveyor, vol. 44, no. 1, pp. 64—70, 1999.
21. Zhang Z X, Zhang J Q, “Digital Photogrammetry,” Wuhan University Press, 1997.